







Varstrometry for Off-nucleus and Dual sub-Kpc AGN (VODKA): Long-slit optical spectroscopic follow-up with Gemini/GMOS and HST/STIS

YU-CHING CHEN ^{1,2} ARRAN C. GROSS ² XIN LIU ^{2,3} YUE SHEN ^{2,3} NADIA L. ZAKAMSKA ¹
HSIANG-CHIH HWANG ⁴ AND MING-YANG ZHUANG ²

¹*Department of Physics and Astronomy, Johns Hopkins University, Baltimore, MD 21218, USA*

²*Department of Astronomy, University of Illinois at Urbana-Champaign, Urbana, IL 61801, USA*

³*National Center for Supercomputing Applications, University of Illinois at Urbana-Champaign, Urbana, IL 61801, USA*

⁴*School of Natural Sciences, Institute for Advanced Study, Princeton, 1 Einstein Drive, NJ 08540, USA*

ABSTRACT

We present Gemini/GMOS and HST/STIS optical spectra for 27 dual quasar candidates selected based on their variability-induced astrometric noise or double detections in Gaia (the VODKA project). From this follow-up, we spectroscopically identify 10 star superpositions and 8 dual/lensed quasars. Among the remaining targets, 2 are likely dual/lensed quasars based on additional radio imaging, while the rest are quasars with unknown companions. Notably, WISE J1649+0812 is a newly confirmed dual quasar with a projected separation of 5 kpc at $z = 1.39$ and a significant velocity offset of 183 ± 76 km/s, highlighting the utility of narrow emission lines in identifying genuine dual quasars. Without prior photometric or spectroscopic selection, we find the star contamination rate to be 37-63%, while the dual/lensed quasar fraction is $\gtrsim 30\%$ in the follow-up VODKA sample. However, when combined with existing unresolved spectra and spatially-resolved two-band color cuts, the dual/lensed quasar fraction can be increased to $\gtrsim 67\%$. High signal-to-noise ratio spectra ($\gtrsim 20$ per spectral element) with adequate spectral resolution ($R \gtrsim 1000$) are essential for identifying faint absorption lines in foreground stars and detecting dual quasars through velocity offsets.

Keywords: Spectroscopy (1558) – Double quasars (406) — Quasars (1319) — Active galactic nuclei (16) — Supermassive black holes (1663) — Strong gravitational lensing (1643)

1. INTRODUCTION

Most nearby massive galaxies harbor a supermassive black hole (SMBH) at their centers (Magorrian et al. 1998; Kormendy & Ho 2013). Cold dark matter models often depict hierarchical structure formation and galaxy mergers (White & Frenk 1991; Navarro et al. 1996; Cole et al. 2000). When two galaxies merge, gas and dust may accrete onto the SMBHs through non-asymmetric gravitational potentials (Barnes & Hernquist 1996), causing the SMBHs to become active and transform into quasars. If both SMBHs are active and still within their host galaxies' potential, they are known as dual quasars. While cosmological simulations show increased quasar activity and dual quasar fraction in the late-stage merg-

ers (Chen et al. 2023a), the observational evidence for the link between quasar activity and mergers is still debated (Mechtley et al. 2016; Fan et al. 2016; Ellison et al. 2019; Breiding et al. 2024). The dual quasar phase is an excellent stage to study quasar triggering and its connection to galaxy mergers (Volonteri et al. 2022).

Identifying dual quasars is challenging due to their rarity and close separations, particularly at higher redshifts ($z > 1$) when the angular diameter distance is large ($1'' \sim 8$ kpc at $z \sim 2$). In recent years, large sky surveys with high angular resolution, such as Gaia, have become valuable tools for finding dual and lensed quasars (Lemon et al. 2018, 2019; Chen et al. 2022; Lemon et al. 2023). Despite the introduction of various techniques to discover small-separation ($\lesssim 1''$) dual quasar candidates (Mannucci et al. 2022; Hwang et al. 2020), only a small fraction of these candidates have been confirmed (Chen et al. 2023b; Mannucci et al. 2023; Ciurlo et al. 2023). One notable effort in finding close-separation

dual quasars is the Varstrometry for Off-nucleus and Dual sub-Kpc AGN (VODKA) project (Hwang et al. 2020; Shen et al. 2019a). The VODKA project aims to discover unresolved dual quasars by analyzing centroid jitters from the non-coherent quasar light from two sources. With dozens of dual quasar candidates discovered by the VODKA project, spectroscopic follow-ups are essential to confirm their nature (Chen et al. 2022).

In this paper, we present optical spectroscopic observations for 27 targets from the VODKA project. We provide classifications based on spectra from the Hubble Space Telescope (HST) and the Gemini Observatory, along with other auxiliary data. The paper is organized as follows. Section 2 describes the data reduction and analysis procedures, as well as the spectral fitting details. In section 3, we show the HST and Gemini spectra for the 27 targets and provide our best classifications. Section 4 discusses the sample category breakdown and the physical properties of the newly discovered dual quasar, J1649+0812, and explores the implications for future spectroscopic observations. We summarize our findings in section 5. We adopt a flat Λ CDM cosmology with $\Omega_\Lambda = 0.7$, $\Omega_m = 0.3$, and $H_0 = 70 \text{ km s}^{-1} \text{ Mpc}^{-1}$ throughout this paper.

2. OBSERVATIONS, DATA REDUCTION AND ANALYSIS

2.1. Target selection: dual quasar candidates

The 27 targets in this paper are the dual/lensed quasar candidates with small separations ($<1''$) discovered using Gaia astrometry and HST images (Chen et al. 2022). The sample consists of 14 Gaia-resolved targets with separations $\gtrsim 0''.5$ and 13 Gaia-unresolved targets selected by the astrometric technique, Varstrometry. The Varstrometry technique utilizes quasar’s strong variability and the non-synchronized emission of two nuclei to discover unresolved dual quasars (Hwang et al. 2020; Shen et al. 2019a). To confirm the nature of these candidates, we conducted a series of spectroscopic follow-up observations using HST and the Gemini Observatory. In addition to the spectroscopic campaign, we carried out imaging programs with the Very Large Array in radio and HST in the near-infrared to detect lens galaxies, study tidal features, and investigate radio properties. These findings are reported in a companion paper (Gross et al. 2024).

2.2. HST/STIS

Out of 27 targets, 22 were observed with HST using the Space Telescope Imaging Spectrograph (STIS) during cycles 28 and 29 in 2021-2022 under programs GO-16210 and GO-16887 (PI: X. Liu). All

the HST data used in this paper can be found in MAST: [10.17909/a3ac-ny86](https://mast.stsci.edu/obj/showImage.do?imageId=10.17909/a3ac-ny86). The observations utilized the G750L grating with a $52'' \times 0.2''$ aperture, covering observed wavelengths from 5240\AA to 10270\AA , with a resolving power of $R \sim 500$. The slit direction was rotated to capture both nuclei, guided by the HST-resolved images (Chen et al. 2022). Exposure times and additional observational details can be found in Table 1.

The STIS spectra were reduced using the `stis_cti` package, which corrects for trails and artifacts caused by charge transfer inefficiency effects (Anderson & Bedin 2010). Following the standard STIS calibration pipeline, `calstis`, we applied flat-field correction, bad-pixel removal, and cosmic ray rejection. The final one-dimensional (1D) spectra for each nucleus were extracted using a boxcar aperture of 7 pixels ($0''.35$). Figure 1 and Figure 2 present the calibrated 1D spectra of all the targets observed with HST/STIS.

2.3. Gemini/GMOS

16 targets were observed using the Gemini Multi-Object Spectrographs (GMOS) on both the Gemini-North and Gemini-South telescopes in 2021 and 2022, under several programs (GN-2020A-DD-106, GS-2020A-DD-106, GN-2022A-Q-139, GS-2022A-Q-148; PI: X. Liu, and GN-2020A-Q-232; PI: Y.-C. Chen). The observations used the R150 grating centered around $\sim 700 \text{ nm}$ with slit widths ranging from $0''.5$ to $0''.75$, covering the observed wavelength range of 4000\AA to 10040\AA , with a resolving power R of $\sim 420\text{--}630$. The typical seeing conditions were $\lesssim 0''.75$ (within the 70th percentile in optical), and for targets with smaller separations ($<0''.5$), seeing was $\lesssim 0''.4$ (within the 20th percentile in optical). Although photometric cloud conditions were not required, most targets were observed under photometric conditions, with no significant signal loss due to clouds. As with the HST/STIS spectra, the slit direction was rotated to capture both nuclei. Standard stars EG131, LTT1788, Wolf1346, and LTT4816 were observed with a similar setup for flux calibration. The exposure times and additional observational details are provided in Table 1.

We reduced the raw exposures using the Python wrapper of the `iraf` software. We perform bias subtraction and flat-field correction. Wavelength calibration was completed using arc exposures taken with the same configuration, and flux calibration was based on standard star exposures with the same grating. We dithered the exposures along both the spatial and spectral directions. The final 2D exposures were combined to eliminate artifacts, remove bad pixels, and fill detector gaps.

The typical seeing conditions for the Gemini observations ranged from $0''.5$ to $0''.8$, comparable to the nuclear separations of our targets. Since many of the targets were only marginally resolved, we opted for a two-component Gaussian fit rather than boxcar extraction. At each spectral element, we fit two Gaussian components with fixed separations along the spatial direction, allowing the centroids and FWHMs to vary initially to account for distortions and seeing variations across the spectral direction. The centroids and FWHMs were then refitted with a cubic spline function. Final flux densities were derived by fitting two Gaussian components with fixed separations and wavelength-dependent centroids and FWHMs, as determined by the cubic spline fit. [Figure 3](#) presents the calibrated 1D spectra of all the targets observed with Gemini/GMOS.

2.4. Spectral fitting

To derive the physical properties of the confirmed dual quasars, we fit the individual spectra using `PyQSOFit`, a Python-based fitting code developed to measure quasar spectral properties ([Guo et al. 2018](#); [Shen et al. 2019b](#)). The spectral model includes a pseudo-continuum, which combines a power-law, a third-order polynomial, and Fe II emission templates ([Boroson & Green 1992](#); [Vestergaard & Wilkes 2001](#)). Additionally, one or more Gaussian components are fitted to represent the narrow and broad emission lines. Specifically, for J1649+0812, we model the Mg II emission line using one Gaussian for the narrow-line component (defined as having a FWHM $< 1200 \text{ km s}^{-1}$) and up to two Gaussians for the broad-line component (defined as having a FWHM $\geq 1200 \text{ km s}^{-1}$). The [O II] emission line is modeled with a single Gaussian for the narrow-line component. Telluric absorption features are removed and replaced with linear interpolations based on nearby pixels. [Figure 6](#) shows our best-fit 1D spectral models for J1649+0812.

3. RESULTS

3.1. Spatially-resolved spectra

We present the optical spectra of the 27 targets obtained from Gemini/GMOS and HST/STIS in this section. [Figure 1](#) and [Figure 2](#) show the HST/STIS spectra of 22 targets. All targets are spatially resolved in the HST/STIS spectra, benefiting from HST’s high angular resolution ($\sim 0''.075$ at 800 nm). For 80% of the targets, we identify the quasars’ broad emission lines in at least one of the sources. However, given the faintness of our targets ($f_\lambda \lesssim 10^{-16} \text{ erg s}^{-1} \text{ cm}^{-2} \text{ \AA}^{-1}$), the typi-

cal signal-to-noise ratios are $\lesssim 10$, making it challenging to identify stellar absorption lines.

[Figure 3](#) shows the Gemini/GMOS spectra of 16 targets. Using the two-Gaussian component fitting method described in [subsection 2.3](#), we successfully decompose the two sources, even when they are only marginally resolved. Thanks to the higher signal-to-noise ratios compared to the STIS spectra, we can identify not only the broad emission lines from quasars but also the narrow emission lines and absorption lines from star interlopers. For the targets observed in program GS-2022A-Q-148, the spectra are truncated at 7700 \AA due to poor response in one of the CCDs.

3.2. Classifications

Using the spectra from Gemini and HST, we perform the following steps to classify each target:

1. Identify quasars based on their broad emission lines and measure their redshifts.
2. Identify stars by detecting absorption lines, such as NaD, if present
3. For featureless spectra without detected emission or absorption lines, identify quasars using deep radio imaging from [Gross et al. \(2024\)](#).
4. If both sources are quasars and show a significant velocity offset, classify the target as a dual quasar.

Based on the spectra and auxiliary multi-wavelength images, we identify 8 dual/lensed quasars, 9 quasar-star superpositions, and 1 binary star. For the remaining 9 targets, 2 are likely dual/lensed quasars. We are unable to conclusively determine the nature of the other 7 targets but provide our best estimates based on the images and spectra. Each group of targets is discussed in the following subsections.

3.2.1. Binary stars and quasar-star superpositions

We detect at least one stellar absorption line (e.g., NaD, $H\alpha$, CaII) from nearby foreground stars in the following targets:

- J0246+6922: binary star (NaD, TiO).
- J0904+3332: $z = 1.106$ quasar + star (Mg, NaD).
- J1314–4912: $z = 2.295$ quasar + star (NaD).
- J1711-1611: $z = 0.790$ quasar + star (NaD, $H\alpha$).
- J1732–1335: $z = 0.292$ quasar + star ($H\alpha$).
- J1804+3230: $z = 0.504$ quasar + star (NaD, CaII).

Table 1. Observation details for the 27 targets from Gemini and HST.

Abbreviated Name (J2000)	Obs. Date (UT)	Exp. Time (min)	SNR	R	Telescope/Instrument	Grating	Program ID
(1)	(2)	(3)	(4)	(5)	(6)	(7)	(8)
WISE J0241+7801	2022-05-11	40	5,1				
WISE J0246+6922	2021-12-28	39	9,6				
WISE J0536+5038	2021-12-12	30	12,5				
SDSS J0748+3146	2022-01-03	33	2,2				
SDSS J0749+2255	2021-02-16	36	5,2				
SDSS J0753+4247	2022-01-17	31	6,2				
SDSS J0823+2418	2022-01-13	30	7,5	500	HST/STIS	G750L	HST-GO-16210
SDSS J0841+4825	2021-02-10	32	3,3				
SDSS J0904+3332	2021-02-28	36	5,4				
WISE J1613–2644	2021-02-27	36	2,1				
WISE J1755+4229	2022-04-01	35	12,2				
WISE J1852+4833	2021-05-13	36	6,2				
WISE J2048+6258	2021-02-15	39	4,2				
SDSS J2122–0026	2021-08-03	30	4,3				
WISE J0348–4015	2022-07-09	35	2,1				
SDSS J1327+1036	2022-05-28	31	2,1				
SDSS J1648+4155	2022-03-28	35	8,2				
WISE J1649+0812	2022-04-20	33	7,3	500	HST/STIS	G750L	HST-GO-16887
WISE J1711–1611	2022-06-12	32	3,2				
WISE J1937–1821	2022-06-11	34	2,2				
WISE J2050–2947	2022-07-20	31	6,3				
WISE J2218–3322	2022-09-05	34	1,0.3				
SDSS J0841+4825	2020-05-21	31	71,51	420	Gemini/GMOS	R150	GN-2020A-DD-106
SDSS J0904+3332	2020-05-21	31	54,15				
WISE J1314–4912	2020-02-23	31	43,33	420	Gemini/GMOS	R150	GS-2020A-DD-106
WISE J1732–1335	2020-08-13	40	42,34				
WISE J1804+3230	2020-08-14	40	38,35	420	Gemini/GMOS	R150	GN-2020A-Q-232
WISE J1852+4833	2020-07-02	60	52,22				
WISE J1857+7048	2020-07-29	60	40,15				
SDSS J0749+2255	2022-04-20	31	29,19	630			
SDSS J0823+2418	2022-04-20	17	40,36	420			
SDSS J1225+4831	2022-04-20	23	31,24	420	Gemini/GMOS	R150	GN-2022A-Q-139
SDSS J1648+4155	2022-04-21	53	49,14	630			
WISE J1649+0812	2022-04-21	23	42,37	630			
WISE J1711–1611	2022-04-01	23	23,18	420			
WISE J1937–1821	2022-06-11	26	21,18	420	Gemini/GMOS	R150	GS-2022A-Q-148
WISE J2050–2947	2022-06-12	20	33,21	420			
WISE J2218–3322	2022-11-17	40	16,10	630			

NOTE—Column 1: Target name. Column 2: Observation date. Column 3: Exposure time. Column 4: Median signal-to-noise ratio per spectral element for each source. Column 5: Spectral resolution $R = \lambda/\Delta\lambda$. Column 6: Telescope and instrument. Column 7: Grating name. Column 8: Program ID

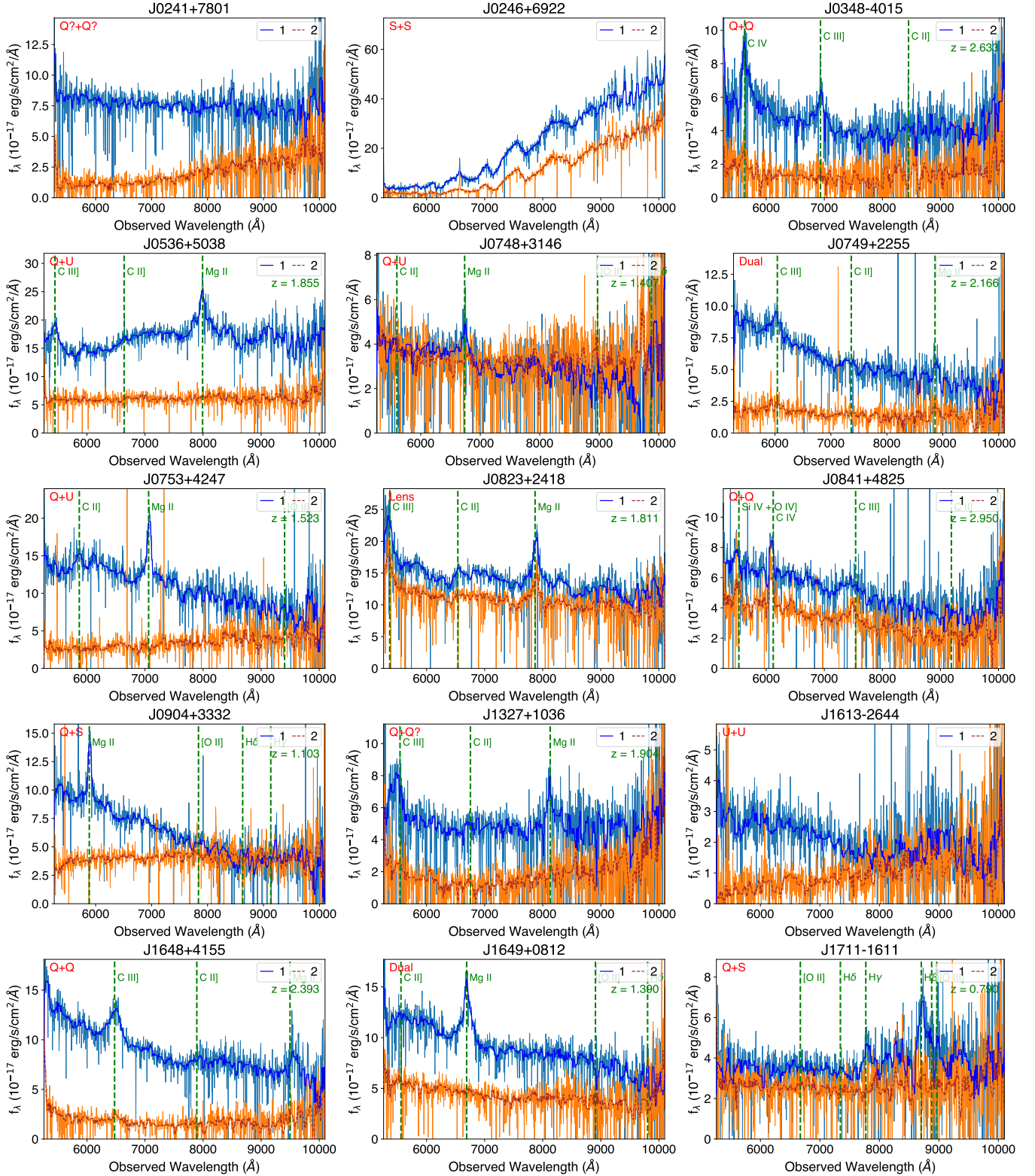


Figure 1. HST STIS optical spectra of 22 targets (15 in this figure and 7 in Figure 2). SSpatially resolved spectra for both sources are shown in solid blue and dashed orange lines. Green vertical lines indicate the quasar’s emission lines at the systemic redshift, displayed in the top-right corner. Final classifications based on both Gemini and/or HST spectra are shown in the top-left corner. (Q: quasar, S: star, U: unknown, Dual: dual quasar, Lens: lensed quasar, ?: likely).

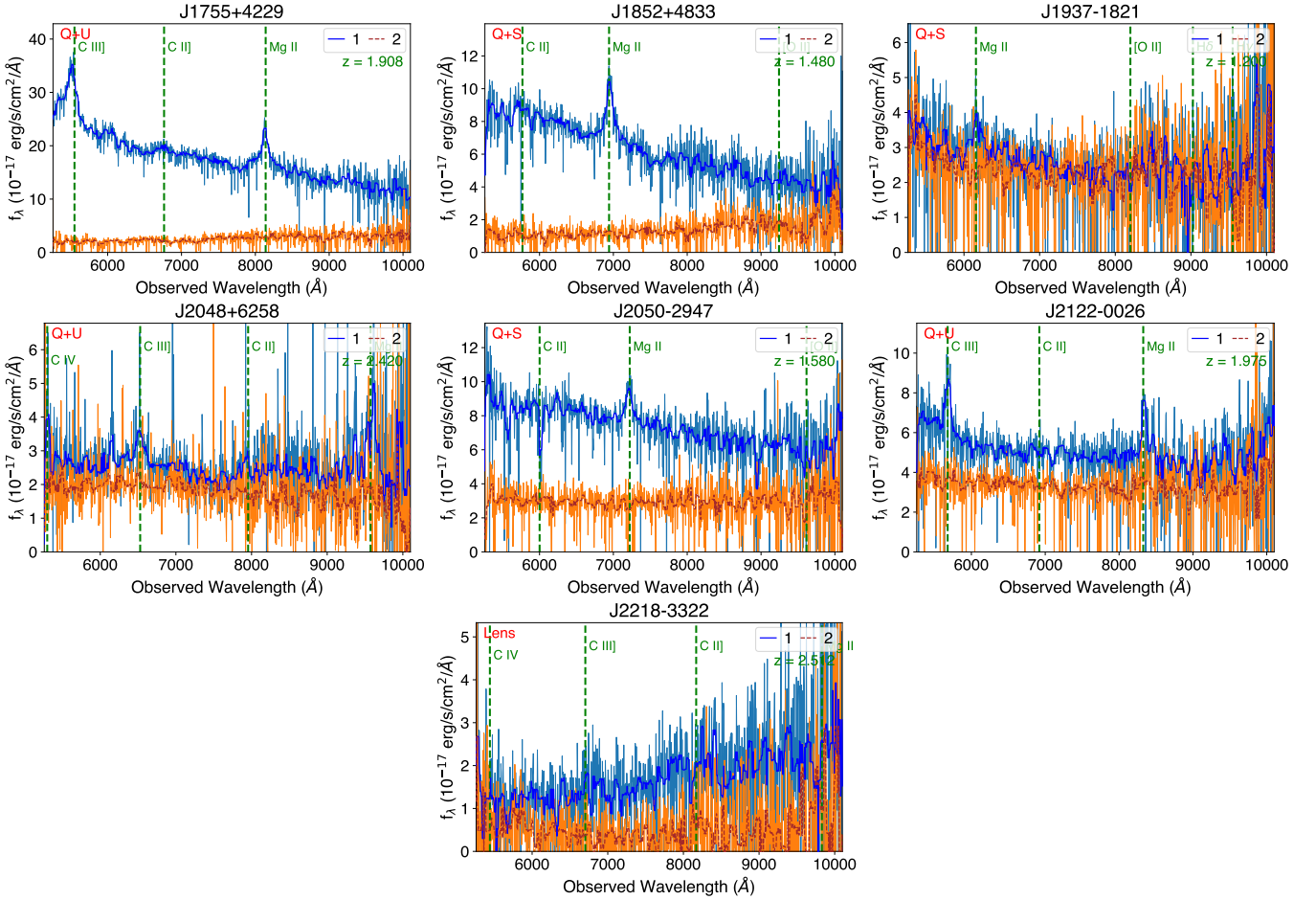


Figure 2. HST STIS optical spectra of 22 targets (7 in this figure and 7 in Figure 1). Notations are the same as those in Figure 1

- J1852+4833: $z = 1.480$ quasar + star (NaD, CaII).
- J1857+7048: $z = 1.230$ quasar + star (NaD, TiO).
- J1937-1821: $z = 1.200$ quasar + star ($H\alpha$).
- J2050-2947: $z = 1.580$ quasar + star (Mg, $H\alpha$).
- J0348–4015: dual/lensed quasar at $z = 2.633$.
- J0749+2255: dual quasar at $z = 2.166$ (Chen et al. 2023b).
- J0823+2418: lensed quasar at $z = 1.811$ (Gross et al. 2023).
- J0841+4825: dual/lensed quasar at $z = 2.940$.
- J1225+4831: dual/lensed quasar at $z = 3.090$.
- J1648+4155: dual/lensed quasar at $z = 2.393$.
- J1649+0812: dual quasar at $z = 1.3902$ and $z = 1.3887$ (velocity offset of 183 ± 76 km/s, Figure 5).
- J2218–3322: quadruply lensed broad absorption line quasar at $z = 2.550$ (Chen et al. 2022).

3.2.2. Dual/lensed quasars

For the following targets, we detect broad emission lines in both sources. Distinguishing between dual quasars and lensed quasars is challenging because the spectra of both sources in most of our dual/lensed quasar candidates are very similar. For example, J0749+2255 and J0823+2418 were confirmed as a dual quasar and a lensed quasar, respectively, based on additional multi-wavelength observations (Chen et al. 2023b; Gross et al. 2023). However, without distinct evidence such as a velocity offset from a narrow emission line, we do not differentiate between dual and lensed quasars in this paper. The classifications are listed below.

Figure 4 shows the median-normalized spectra of the 8 dual/lensed quasars, highlighting the similarities and differences between the two spectra for each system.

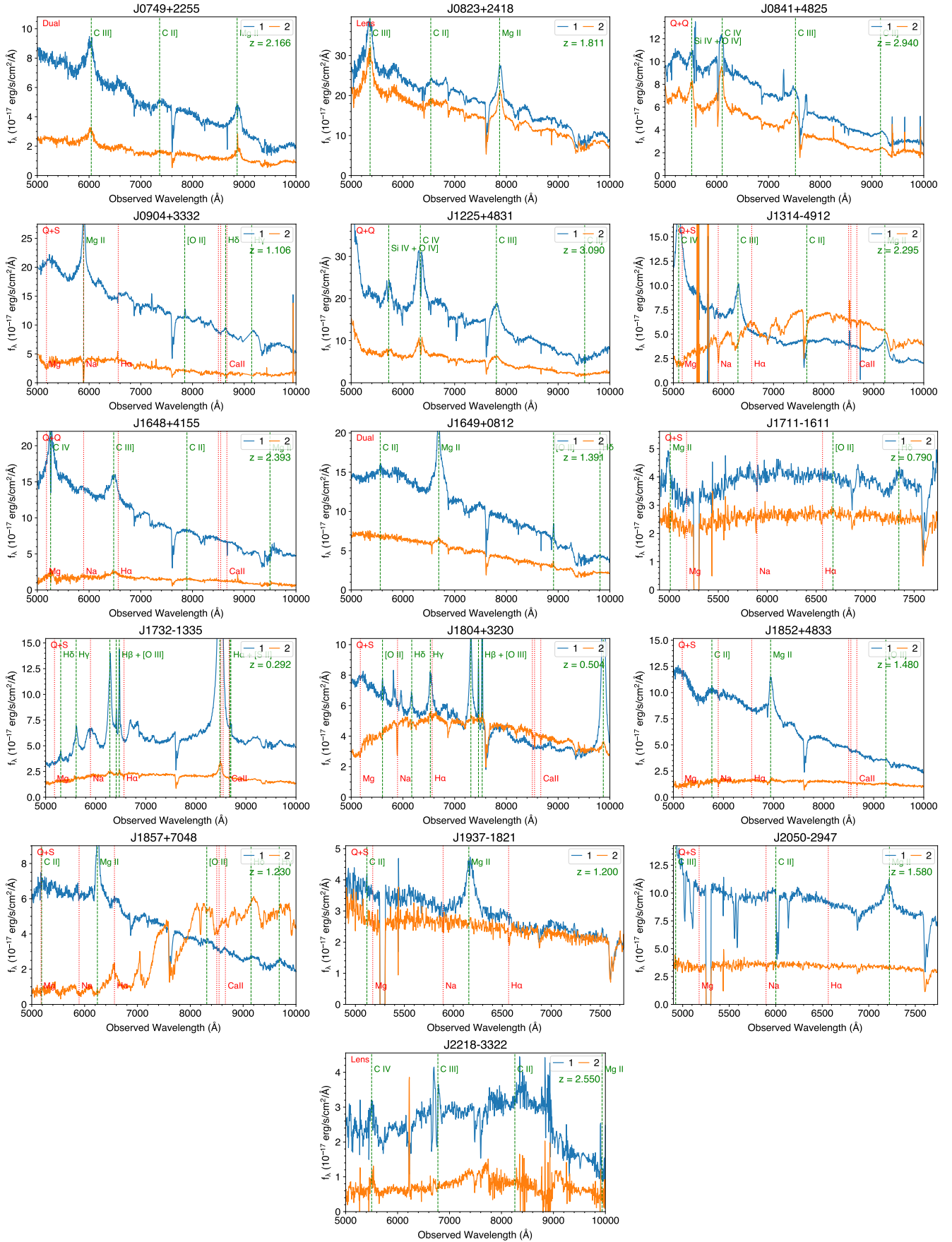


Figure 3. Gemini GMOS optical spectra of 16 targets. Spatially resolved spectra for both sources are shown in solid blue and dashed orange lines. Green vertical lines mark the quasar’s emission lines at the systemic redshift, displayed in the top-right corner. Red vertical lines indicate stellar absorption features for star superposition. Final classifications based on both Gemini and/or HST spectra are shown in the top-left corner (Q: quasar, S: star, U: unknown, Dual: dual quasar, Lens: lensed quasar, ?: likely).

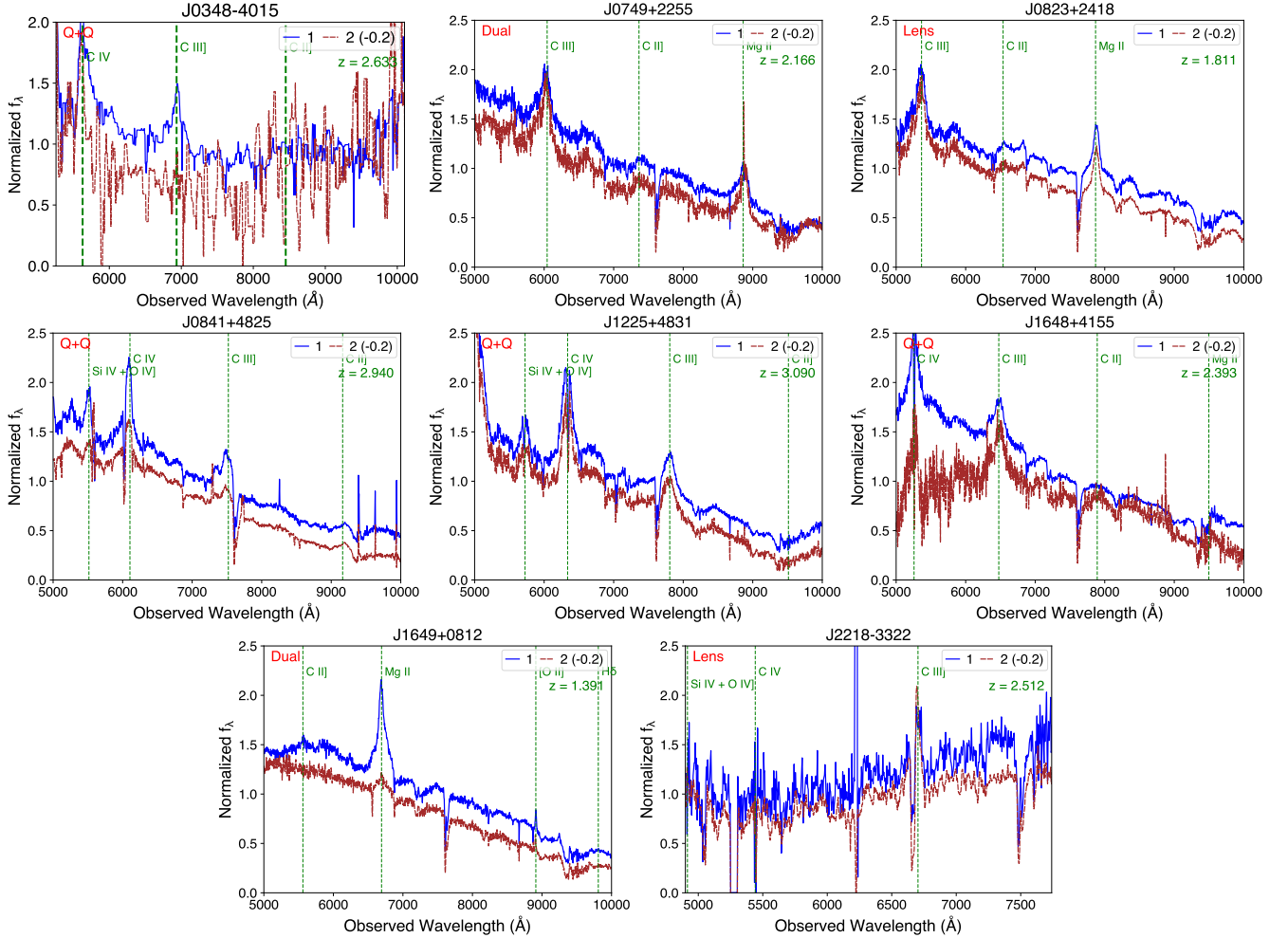


Figure 4. Median-normalized spectra of the 8 dual/lensed quasars, with the second source spectra shifted by -0.2 to prevent overlap. Spatially resolved spectra for both sources are represented by solid blue and dashed brown lines. Quasar emission lines at the corresponding redshift (indicated in the top-right corner) are marked by green vertical lines.

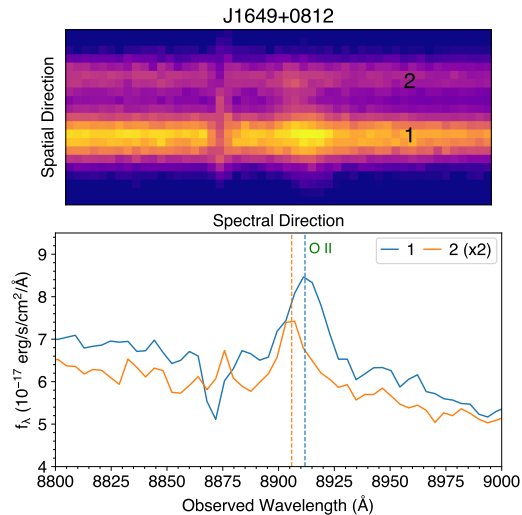


Figure 5. Top: 2D spectrum of J1649+0812 showing the traces of two sources and the [O II] emission. Bottom: Extracted 1D spectra of J1649+0812 showing the velocity offset of 200 km/s between two sources.

3.2.3. Unknown cases

For the 9 remaining targets, we either detect only one broad emission line or are unable to identify any emission or absorption lines. We also examine radio observations for some targets (Gross et al. 2024) to identify potential obscured quasars.

- J0241+7801: Both sources are likely quasars with unknown redshifts. Source 1 shows a possible emission line at 8500 Å, while Source 2 has a radio detection of $>2\text{mJy}$ (Gross et al. 2024).
- J0536+5038: $z = 1.855$ quasar + unknown source.
- J0748+3146: $z = 1.407$ quasar + unknown source.
- J0753+4247: $z = 1.523$ quasar + unknown source.
- J1327+1036: $z = 1.904$ quasar + a likely quasar. Both sources are detected in radio with $\sim \text{mJy}$ scales (Gross et al. 2024).
- J1613-2644: Unknown case. No emission lines are detected in both sources.
- J1755+4229: $z = 1.908$ quasar + unknown source.
- J2048+6258: $z = 2.420$ quasar + unknown source.
- J2212-0026: $z = 1.975$ quasar + unknown source.

4. DISCUSSION

4.1. Quasar-star-superposition and dual/lensed quasar fractions

Based on the 2-band color cut using HST F475W and F814W images, Chen et al. (2022) estimated a quasar-star superposition rate of $30\% \pm 10\%$ for the targets in the VODKA project. However, this simple 2-band color cut method primarily differentiates late-type stars from typical unobscured quasars, potentially misclassifying early-type stars and obscured quasars. With our spectroscopic follow-up observations, we can now provide a more accurate assessment of the fractions of star superpositions and dual/lensed quasars.

Among the 45 targets discovered in the VODKA imaging project (Chen et al. 2022) and additional targets from various subsequent campaigns, we observed 25 with our spectroscopic data. For these observed targets, we calculated a star superposition rate of $10/27 = 37\%$. This is likely a lower limit because we selectively followed up on targets with blue and similar colors, and additional quasar-star superpositions may be present among the uncertain cases. Assuming that targets with unknown companions are all quasar-star superpositions, the upper limit of the quasar-star superposition rate is $17/27 = 63\%$. This 37-63% superposition rate exceeds the estimated rate of $30\% \pm 10\%$ from the two-band color cut (Chen et al. 2022). The higher rate is likely due to the exclusion of stars (e.g., F and G stars) with similar optical colors to quasars in the two-band color cut. For dual/lensed quasars, counting only those confirmed spectroscopically from spatially resolved spectra, we obtained a fraction of $8/27 = 30\%$. This fraction is a lower limit, as additional dual/lensed quasars might not have been discovered due to low signal-to-noise spectra or because they were not observed due to redder colors.

We can evaluate whether additional selection criteria could yield a cleaner sample. For instance, if we restrict our candidates to those identified as spectroscopically confirmed quasars, and apply the same reasoning as before, we find that the quasar-star superposition rate ranges from $1/10 = 10\%$ to $4/10 = 40\%$. Additionally, the lower limit for the fraction of dual/lensed quasars increases to $5/10 = 50\%$.

We can examine whether extra selection criteria can provide a cleaner sample. For example, if we only select candidates from spectroscopically confirmed quasars and following the same argument in the previous paragraph, we can obtain the quasar-star superposition rate between $1/10 = 10\%$ and $4/10 = 40\%$, and the lower limit of dual/lensed quasar fraction is $5/10 = 50\%$. Similar calculations can be performed by considering only

Table 2. Properties and classifications of the 27 targets

Abbreviated Name (J2000)	R.A. (deg)	Decl. (deg)	Target Category	Color Selection	Spectroscopic Classification
(1)	(2)	(3)	(4)	(5)	(6)
WISE J0241+7801	40.395481	78.018624	2	quasar+star	likely quasar+quasar
WISE J0246+6922	41.619305	69.376122	5	quasar+star	binary star
WISE J0348−4015	57.119449	−40.253662	3	dual/lensed quasar	dual/lensed quasar(z=2.633)
WISE J0536+5038	84.084298	50.6406250	2	dual/lensed quasar	quasar(z=1.855) + unknown
SDSS J0748+3146	117.002307	31.779856	4	dual/lensed quasar	quasar(z=1.407) + unknown
SDSS J0749+2255	117.345694	22.919936	1	dual/lensed quasar	dual quasar(z=2.166)
SDSS J0753+4247	118.460738	42.795529	1	quasar+star	quasar(z=1.523) + unknown
SDSS J0823+2418	125.921169	24.301570	4	dual/lensed quasar	lensed quasar(z=1.811)
SDSS J0841+4825	130.374046	48.430135	1	dual/lensed quasar	dual/lensed quasar(z=2.940)
SDSS J0904+3332	136.036118	33.534796	1	quasar+star	quasar(z=1.106) + star
SDSS J1225+4831	186.327776	48.521147	4 ^a	... ^a	dual/lensed quasar(z=3.090)
WISE J1314−4912	198.566742	−49.205070	6	quasar+stars	quasar(z=2.295) + star
SDSS J1327+1036	201.966887	10.607564	1 ^a	... ^a	quasar(z=1.904)+ likely quasar
WISE J1613−2644	243.456316	−26.742377	2	quasar+star	unknown
SDSS J1648+4155	252.075328	41.930608	1	dual/lensed quasar	dual/lensed quasar(z=2.393)
WISE J1649+0812	252.422063	8.209311	5	dual/lensed quasar	dual quasar(z=1.3902,1.3887)
WISE J1711−1611	257.916584	−16.196649	5	dual/lensed quasar	quasar(z=0.790) + star
WISE J1732−1335	263.095334	−13.593137	2	dual/lensed quasar+star	quasar(z=0.292) + star
WISE J1755+4229	268.929920	42.490069	5	quasar+star	quasar(z=1.908) + unknown
WISE J1804+3230	271.039815	32.508215	5	quasar+star	quasar(z=0.504) + star
WISE J1852+4833	283.108771	48.554173	2	quasar+star	quasar(z=1.480) + star
WISE J1857+7048	284.369408	70.803154	5	quasar+star	quasar(z=1.230) + star
WISE J1937−1821	294.328398	−18.358950	2	dual/lensed quasar	quasar(z=1.200) + star
WISE J2048+6258	312.200003	62.98286	5	dual/lensed quasar	quasar(z=2.420) + unknown
WISE J2050−2947	312.500061	−29.789362	5	dual/lensed quasar	quasar(z=1.580) + star
SDSS J2122−0026	320.679218	−0.448282	4	dual/lensed quasar	quasar(z=1.975) + unknown
WISE J2218−3322	334.707755	−33.378782	5	quad lens	quad lens(z=2.512)

NOTE—Column 1: Target name. Column 2: Right Ascension. Column 3: Declination. Column 4: Target category from [Chen et al. \(2022\)](#) (1: SDSS Gaia-unresolved, 2: WISE+PS1 Gaia-unresolved, 3: WISE-only Gaia-unresolved, 4: SDSS Gaia-resolved, 5: WISE+PS1 Gaia-resolved, 6: WISE-only Gaia-resolved). Column 5: Photometric classification using HST F475W and F814W images from [Chen et al. \(2022\)](#). Column 6: Spectroscopic classification based on the optical spectra in this paper

^aJ1225+4831 and J1327+1036 were not observed in HST snapshot imaging program ([Chen et al. 2022](#)), but they were discovered using the same VODKA technique.

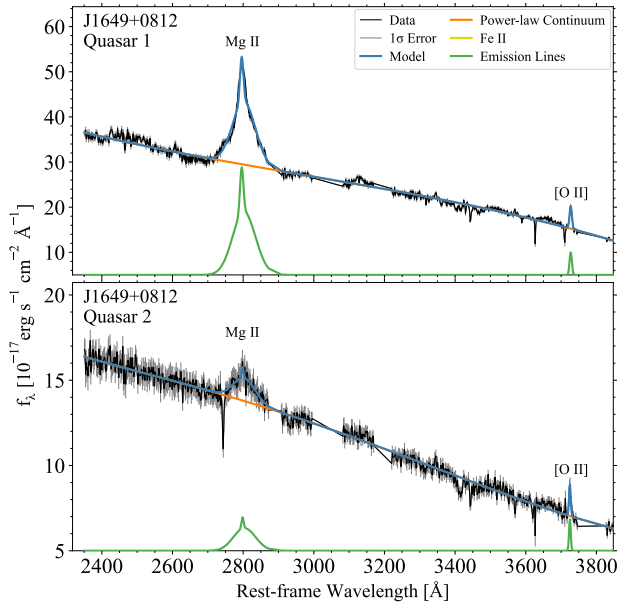
the targets classified as dual/lensed quasar candidates using HST F475W and F814W images ([Chen et al. 2022](#)). The quasar-star superposition and dual/lensed quasar fractions for various samples are listed in [Table 3](#). In summary, with existing unresolved spectra from SDSS and the spatially resolved two-band color cut, the fraction of dual/lensed quasars can be pushed to higher than 67%.

4.2. Physical properties of the dual quasar J1649+0812

To obtain the physical properties of the newly discovered dual quasar, J1649+0812, we fit the spectra using `PyQSOFit`, as detailed in [subsection 2.4](#). The measurements of the continuum and emission lines are listed in [Table 4](#), and the fitted models are shown in [Figure 6](#). The measurements of Mg II is used to estimate the BH masses. We estimate the single-epoch virial BH masses

Table 3. Fraction of quasar-star superpositions and dual/lensed quasars

Sample	#	Dual/lens	Quasar-star
(1)	(2)	(3)	(4)
1. Whole follow-up sample	25	$\gtrsim 30\%$	$\sim 37\text{-}63\%$
2. SDSS quasars only	10	$\gtrsim 50\%$	$\sim 10\text{-}40\%$
3. F475W-F814W color cut	15	$\gtrsim 47\%$	$\sim 27\text{-}53\%$
4. Criteria 2 and 3	6	$\gtrsim 67\%$	$\sim 0\text{-}33\%$

 NOTE—Column 1: Sample selection. Column 2: Number of targets. Column 3: Dual/lensed quasar fraction 4: Quasar-star superposition fraction. F475W-F814W color cut is mainly based on the photometric classification in [Chen et al. \(2022\)](#).

Figure 6. Spectral fitting of the dual quasar, J1649+0812, using PyQSOfit. Shown are the data (black), the 1σ rms error (gray), the best-fit model (blue), the power-law plus polynomial model for the emission-line-subtracted continuum (orange), and the emission lines (green).

using the following relation:

$$\log\left(\frac{M_{\text{BH}}}{M_{\odot}}\right) = a + b \log\left(\frac{\lambda L_{\lambda}}{10^{44} \text{ erg s}^{-1}}\right) + 2 \log\left(\frac{\text{FWHM}}{\text{km s}^{-1}}\right), \quad (1)$$

where $a = 0.85$, $b = 0.5$ ([Vestergaard & Osmer 2009](#)) and λL_{λ} is the continuum luminosity at restframe 3000 Å, while FWHM is the full width at half maximum of the Mg II line. The systematic error of the single-epoch virial BH mass estimation is 0.4 dex ([Shen et al. 2013](#)). The estimated BH masses of J1649+0812 are $10^{9.1 \pm 0.4}$

and $10^{9.4 \pm 0.4} M_{\odot}$. We calculate the quasar’s bolometric luminosity using the monochromatic luminosity at 3000 Å and applying bolometric correction factors from [Richards et al. \(2006\)](#). Assuming an isotropic radiation distribution, the bolometric luminosity, L_{bol} , can be estimated as:

$$L_{\text{bol}} = \lambda L_{\lambda} \times BC, \quad (2)$$

where $BC = 5.62$ is the bolometric correction for the restframe 3000Å continuum luminosity ([Richards et al. 2006](#)). The bolometric luminosities L_{bol} are $5.4 \pm 1.1 \times 10^{46} \text{ ergs s}^{-1}$ and $2.5 \pm 0.5 \times 10^{46} \text{ ergs s}^{-1}$. The Eddington luminosity, L_{Edd} , can be estimated from the black hole mass using the relation:

$$L_{\text{Edd}} \sim 1.26 \times 10^{38} \left(\frac{M_{\text{BH}}}{M_{\odot}}\right) \text{ ergs}^{-1}. \quad (3)$$

where M_{BH} is the black hole mass in solar masses. This allows us to determine the Eddington ratios for both sources. The Eddington ratios, $\log(L_{\text{bol}}/L_{\text{Edd}})$, are -0.42 ± 0.41 and -1.15 ± 0.43 , which are consistent with the typical values observed in single quasars, as seen in the Eddington ratio distribution function ([Kelly et al. 2010](#)).

The [O II] $\lambda 3727$ luminosity is commonly used as a star formation rate (SFR) tracer for objects at redshift $z > 0.4$ where H α is shifted outside the optical range ([Gallagher et al. 1989](#); [Rosa-González et al. 2002](#); [Kewley et al. 2004](#); [Zhuang & Ho 2019, 2020](#)). However, the [O II]-based SFR is subject to dust reddening and chemical abundance and is considered less precise compared with the H α -based SFR ([Jansen et al. 2001](#); [Kewley et al. 2004](#)). Additionally, low-ionization forbidden emission lines, such as [O II], are often influenced by quasar ionization ([Zakamska et al. 2016](#)). Therefore, before calculating the SFR using [O II] luminosities, it is necessary to assess the contribution of quasar ionization to the [O II] emission.

[Zhuang & Ho \(2019\)](#) used radiation pressure-dominated photoionization models to constrain [O II] luminosities from quasar narrow-line regions, and we follow a similar approach. The [O II] luminosity can be estimated from the [O III] luminosity using the relation:

$$L_{[\text{O II}]} = 0.109^{+0.016}_{-0.006} L_{[\text{O III}]}. \quad (4)$$

This assumes that the cloud is radiation pressure-dominated ([Zhuang & Ho 2019](#)). Although we lack [O III] luminosities for J1649+0812, we can estimate them from the bolometric luminosity using the relationship $L_{\text{bol}} = (600 \pm 150)L_{[\text{O III}]}$, as suggested by [Kauffmann & Heckman \(2009\)](#). The estimated [O II] luminosities from the quasar narrow-line region are $9.8 \pm 3.5 \times 10^{42}$ and $4.5 \pm 1.6 \times 10^{42} \text{ ergs s}^{-1}$. Despite

Table 4. Physical properties of dual quasar J1649+0812. Listed from left to right are: abbreviated name, angular separation, projected physical separation, velocity offsets between the two quasars, FWHM of the broad Mg II lines, continuum luminosities at restframe 3000 Å, BH masses, Eddington ratios, and [O II] luminosities.

Object	Sep.	r_p	Δv	FWHM _{Mg II}	$\lambda L_{\lambda,3000}$	$\log(\frac{M_{\text{BH}}}{M_{\odot}})$	$\log(\frac{L_{\text{bol}}}{L_{\text{Edd}}})$	$L_{[\text{O II}]}$
(1)	(arcsec)	(kpc)	(km s ⁻¹)	(km s ⁻¹)	(ergs s ⁻¹)	(7)	(8)	(10 ⁴² ergs s ⁻¹)
WISE J1649+0812-1	0.59	5.0	183±76	3962±201	9.48×10 ⁴⁵	9.06±0.40	-0.42±0.41	5.22±0.24
WISE J1649+0812-2				7586±1236	4.41×10 ⁴⁵	9.44±0.42	-1.15±0.43	1.28±0.18

the large uncertainties, these estimates are two to three times higher than the observed values, indicating that [O II] emission is heavily dominated by quasar photoionization and, therefore, cannot be used as a reliable SFR indicator for J1649+0812.

4.3. Implication for future spectroscopic follow-ups

Based on the results of this study, we outline the following implications for future spectroscopic follow-up to confirm the nature of dual quasar candidates:

- Given the high star-superposition rate (37–63%), we suggest performing detailed spectral decomposition for targets with existing spectra (e.g., SDSS) before conducting follow-up observations. Shen et al. (2023) successfully used spectral principal component analysis to identify potential star superpositions, revealing star companions of various types. Applying similar spectral decomposition to existing spectra can help reduce the star-superposition rate and better allocate limited telescope time to higher-confidence dual/lensed quasar candidates.
- A decent signal-to-noise ratio for the continuum is essential to detect absorption lines such as NaD, H α , and MgI, particularly for F and G type stars. We recommend an signal-to-noise ratio of $\gtrsim 20$ per spectral element. In our data, the Gemini spectra achieve an signal-to-noise ratio of at least ~ 20 per spectral element, whereas the HST/STIS spectra range from 1 to 10 per spectral element.
- Higher spectral resolution may be necessary to accurately identify velocity offsets in dual quasars. With a signal-to-noise ratio of ~ 10 for narrow emission lines, such as [O II] in our case, we only achieved a 3σ detection for a velocity offset of 180 km/s due to our spectral resolution of $R = 630$ (which corresponds to 480 km/s). To better resolve the radial velocities of two quasars, we recommend using higher spectral resolution, such as $R \sim 1000$ (corresponding to 300 km/s).

5. CONCLUSION

In this paper, we present extensive spectroscopic follow-up observations for 27 dual quasar candidates identified by the VODKA project. Using data from the Gemini/GMOS and HST/STIS instruments, we classify and confirm the nature of these candidates. We identify 10 star superpositions and 8 dual/lensed quasars. For the remaining 9 targets, conclusive classifications can not be made, although 2 are likely dual quasars based on auxiliary radio images. Among the 8 dual/lensed quasars, 3 had been previously reported as dual or lensed quasars, and J1649+0812 is a newly confirmed dual quasar at $z = 1.39$ with a significant velocity offset of 180 km/s, as indicated by [O II]. The black hole masses of J1649+0812 are estimated to be $10^{9.1}$ and $10^{9.4} M_{\odot}$, with Eddington ratios of -0.42 ± 0.41 and -1.15 ± 0.43 . We find that the [O II] emission in J1649+0812 is likely dominated by quasar contributions and is not suitable for star formation rate calculations.

Our follow-up observations yield a star-superposition rate of 37–63% in the VODKA sample, which exceeds previous estimates. The fraction of dual/lensed quasars is at least 30%. The higher quasar-star superposition rate is likely due to the lack of initial color selection or spectral decomposition for the VODKA sample. By leveraging unresolved SDSS spectra and spatially resolved two-band color cuts, we estimate that the dual/lensed quasar fraction could exceed 67%. The ongoing HST snapshot program (Program ID: SNAP-17455; PI: Shen) incorporates various selection criteria to obtain a cleaner sample of dual/lensed quasar candidates. Further multi-wavelength observations and detailed analysis of narrow emission lines are necessary to better differentiate between dual and lensed quasars. Our study highlights the critical need for high-quality spectral data with a signal-to-noise ratio of $\gtrsim 20$ and a spectral resolution of $R \gtrsim 1000$ to effectively remove star superpositions and identify dual quasars.

We thank Michael Leveille, Alison Vick, Kristin Chiboucas, Hwi Hyun Kim, Trent Dupuy, Atsuko Nitta, Siyi Xu, and Rodolfo Angeloni for their help with our HST and Gemini observations. This work is supported by NSF grant AST-2108162. Y.S. acknowledges partial support from NSF grant AST-2009947. Support for Program number HST-GO-16210 and HST-GO-16887 (PI: X. Liu) was provided by NASA through grants from the Space Telescope Science Institute, which is operated by the Association of Universities for Research in Astronomy, Incorporated, under NASA contract NAS5-26555. Based on observations made with the NASA/ESA Hubble Space Telescope, obtained from the Data Archive at the Space Telescope Science Institute, which is operated by the Association of Universities for Research in Astronomy, Inc., under NASA contract NAS 5-26555. These observations are associated with programs GO-16210 and GO-16887.

Based in part on observations obtained at the international Gemini Observatory (Program IDs GN-2020A-DD-106, GN-2022A-Q-139, and GS-2022A-Q-148; PI: X. Liu, and GN-2020A-Q-232; PI: Y.-C. Chen), a program of NSF’s NOIRLab, which is managed by the Association of Universities for Research in Astronomy (AURA) under a cooperative agreement with the National Science Foundation. on behalf of the Gemini Observatory partnership: the National Science Foundation (United States), National Research Council (Canada), Agencia Nacional de Investigación y Desarrollo (Chile), Ministerio de Ciencia, Tecnología e Innovación (Argentina), Ministério da Ciência, Tecnologia, Inovações e Comunicações (Brazil), and Korea Astronomy and Space Science Institute (Republic of Korea). This work was enabled by observations made from the Gemini North telescope, located within the Maunakea Science Reserve and adjacent to the summit of Maunakea. We are grateful for the privilege of observing the Universe from a place that is unique in both its astronomical quality and its cultural significance.

Facilities: HST(STIS), Gemini(GMOS)

Software: `numpy` (Harris et al. 2020), `astropy` (Astropy Collaboration et al. 2013, 2018, 2022), `PyQSOFit`(Guo et al. 2018)

REFERENCES

- Anderson, J., & Bedin, L. R. 2010, *PASP*, 122, 1035, doi: [10.1086/656399](https://doi.org/10.1086/656399)
- Astropy Collaboration, Robitaille, T. P., Tollerud, E. J., et al. 2013, *A&A*, 558, A33, doi: [10.1051/0004-6361/201322068](https://doi.org/10.1051/0004-6361/201322068)
- Astropy Collaboration, Price-Whelan, A. M., Sipőcz, B. M., et al. 2018, *AJ*, 156, 123, doi: [10.3847/1538-3881/aabc4f](https://doi.org/10.3847/1538-3881/aabc4f)
- Astropy Collaboration, Price-Whelan, A. M., Lim, P. L., et al. 2022, *ApJ*, 935, 167, doi: [10.3847/1538-4357/ac7c74](https://doi.org/10.3847/1538-4357/ac7c74)
- Barnes, J. E., & Hernquist, L. 1996, *ApJ*, 471, 115, doi: [10.1086/177957](https://doi.org/10.1086/177957)
- Borson, T. A., & Green, R. F. 1992, *ApJS*, 80, 109, doi: [10.1086/191661](https://doi.org/10.1086/191661)
- Breiding, P., Chiaberge, M., Lambrides, E., et al. 2024, *ApJ*, 963, 91, doi: [10.3847/1538-4357/ad19db](https://doi.org/10.3847/1538-4357/ad19db)
- Chen, N., Di Matteo, T., Ni, Y., et al. 2023a, *MNRAS*, 522, 1895, doi: [10.1093/mnras/stad834](https://doi.org/10.1093/mnras/stad834)

- Chen, Y.-C., Hwang, H.-C., Shen, Y., et al. 2022, *ApJ*, 925, 162, doi: [10.3847/1538-4357/ac401b](https://doi.org/10.3847/1538-4357/ac401b)
- Chen, Y.-C., Liu, X., Foord, A., et al. 2023b, *Nature*, 616, 45, doi: [10.1038/s41586-023-05766-6](https://doi.org/10.1038/s41586-023-05766-6)
- Ciurlo, A., Mannucci, F., Yeh, S., et al. 2023, arXiv e-prints, arXiv:2301.03091, doi: [10.48550/arXiv.2301.03091](https://doi.org/10.48550/arXiv.2301.03091)
- Cole, S., Lacey, C. G., Baugh, C. M., & Frenk, C. S. 2000, *MNRAS*, 319, 168, doi: [10.1046/j.1365-8711.2000.03879.x](https://doi.org/10.1046/j.1365-8711.2000.03879.x)
- Ellison, S. L., Viswanathan, A., Patton, D. R., et al. 2019, *MNRAS*, 487, 2491, doi: [10.1093/mnras/stz1431](https://doi.org/10.1093/mnras/stz1431)
- Fan, L., Han, Y., Fang, G., et al. 2016, *ApJL*, 822, L32, doi: [10.3847/2041-8205/822/2/L32](https://doi.org/10.3847/2041-8205/822/2/L32)
- Gallagher, J. S., Bushouse, H., & Hunter, D. A. 1989, *AJ*, 97, 700, doi: [10.1086/115015](https://doi.org/10.1086/115015)
- Gross, A. C., Chen, Y.-C., Foord, A., et al. 2023, *ApJ*, 956, 117, doi: [10.3847/1538-4357/acf469](https://doi.org/10.3847/1538-4357/acf469)
- Gross, A. C., Chen, Y.-C., Masamune, O., et al. 2024, in prep.
- Guo, H., Shen, Y., & Wang, S. 2018, PyQSOFit: Python code to fit the spectrum of quasars, Astrophysics Source Code Library. <http://ascl.net/1809.008>
- Harris, C. R., Millman, K. J., van der Walt, S. J., et al. 2020, *Nature*, 585, 357, doi: [10.1038/s41586-020-2649-2](https://doi.org/10.1038/s41586-020-2649-2)
- Hwang, H.-C., Shen, Y., Zakamska, N., & Liu, X. 2020, *ApJ*, 888, 73, doi: [10.3847/1538-4357/ab5c1a](https://doi.org/10.3847/1538-4357/ab5c1a)
- Jansen, R. A., Franx, M., & Fabricant, D. 2001, *ApJ*, 551, 825, doi: [10.1086/320228](https://doi.org/10.1086/320228)
- Kauffmann, G., & Heckman, T. M. 2009, *MNRAS*, 397, 135, doi: [10.1111/j.1365-2966.2009.14960.x](https://doi.org/10.1111/j.1365-2966.2009.14960.x)
- Kelly, B. C., Vestergaard, M., Fan, X., et al. 2010, *ApJ*, 719, 1315, doi: [10.1088/0004-637X/719/2/1315](https://doi.org/10.1088/0004-637X/719/2/1315)
- Kewley, L. J., Geller, M. J., & Jansen, R. A. 2004, *AJ*, 127, 2002, doi: [10.1086/382723](https://doi.org/10.1086/382723)
- Kormendy, J., & Ho, L. C. 2013, *ARA&A*, 51, 511, doi: [10.1146/annurev-astro-082708-101811](https://doi.org/10.1146/annurev-astro-082708-101811)
- Lemon, C., Anguita, T., Auger-Williams, M. W., et al. 2023, *MNRAS*, 520, 3305, doi: [10.1093/mnras/stac3721](https://doi.org/10.1093/mnras/stac3721)
- Lemon, C. A., Auger, M. W., & McMahon, R. G. 2019, *MNRAS*, 483, 4242, doi: [10.1093/mnras/sty3366](https://doi.org/10.1093/mnras/sty3366)
- Lemon, C. A., Auger, M. W., McMahon, R. G., & Ostrovski, F. 2018, *MNRAS*, 479, 5060, doi: [10.1093/mnras/sty911](https://doi.org/10.1093/mnras/sty911)
- Magorrian, J., Tremaine, S., Richstone, D., et al. 1998, *AJ*, 115, 2285, doi: [10.1086/300353](https://doi.org/10.1086/300353)
- Mannucci, F., Pancino, E., Belfiore, F., et al. 2022, *Nature Astronomy*, 6, 1185, doi: [10.1038/s41550-022-01761-510.48550/arXiv.2203.11234](https://doi.org/10.1038/s41550-022-01761-510.48550/arXiv.2203.11234)
- Mannucci, F., Scialpi, M., Ciurlo, A., et al. 2023, arXiv e-prints, arXiv:2305.07396, doi: [10.48550/arXiv.2305.07396](https://doi.org/10.48550/arXiv.2305.07396)
- Mechtley, M., Jahnke, K., Windhorst, R. A., et al. 2016, *ApJ*, 830, 156, doi: [10.3847/0004-637X/830/2/156](https://doi.org/10.3847/0004-637X/830/2/156)
- Navarro, J. F., Frenk, C. S., & White, S. D. M. 1996, *ApJ*, 462, 563, doi: [10.1086/177173](https://doi.org/10.1086/177173)
- Richards, G. T., Strauss, M. A., Fan, X., et al. 2006, *AJ*, 131, 2766, doi: [10.1086/503559](https://doi.org/10.1086/503559)
- Rosa-González, D., Terlevich, E., & Terlevich, R. 2002, *MNRAS*, 332, 283, doi: [10.1046/j.1365-8711.2002.05285.x](https://doi.org/10.1046/j.1365-8711.2002.05285.x)
- Shen, Y., Hwang, H.-C., Zakamska, N., & Liu, X. 2019a, *ApJL*, 885, L4, doi: [10.3847/2041-8213/ab4b54](https://doi.org/10.3847/2041-8213/ab4b54)
- Shen, Y., Liu, X., Loeb, A., & Tremaine, S. 2013, *ApJ*, 775, 49, doi: [10.1088/0004-637X/775/1/49](https://doi.org/10.1088/0004-637X/775/1/49)
- Shen, Y., Hall, P. B., Horne, K., et al. 2019b, *ApJS*, 241, 34, doi: [10.3847/1538-4365/ab074f](https://doi.org/10.3847/1538-4365/ab074f)
- Shen, Y., Hwang, H.-C., Oguri, M., et al. 2023, *ApJ*, 943, 38, doi: [10.3847/1538-4357/aca662](https://doi.org/10.3847/1538-4357/aca662)
- Vestergaard, M., & Osmer, P. S. 2009, *ApJ*, 699, 800, doi: [10.1088/0004-637X/699/1/800](https://doi.org/10.1088/0004-637X/699/1/800)
- Vestergaard, M., & Wilkes, B. J. 2001, *ApJS*, 134, 1, doi: [10.1086/320357](https://doi.org/10.1086/320357)
- Volonteri, M., Pfister, H., Beckmann, R., et al. 2022, *MNRAS*, 514, 640, doi: [10.1093/mnras/stac1217](https://doi.org/10.1093/mnras/stac1217)
- White, S. D. M., & Frenk, C. S. 1991, *ApJ*, 379, 52, doi: [10.1086/170483](https://doi.org/10.1086/170483)
- Zakamska, N. L., Lampayan, K., Petric, A., et al. 2016, *MNRAS*, 455, 4191, doi: [10.1093/mnras/stv2571](https://doi.org/10.1093/mnras/stv2571)
- Zhuang, M.-Y., & Ho, L. C. 2019, *ApJ*, 882, 89, doi: [10.3847/1538-4357/ab340d](https://doi.org/10.3847/1538-4357/ab340d)
- . 2020, *ApJ*, 896, 108, doi: [10.3847/1538-4357/ab8f2e](https://doi.org/10.3847/1538-4357/ab8f2e)